Supporting Information for:

Low-Dose Nanoscale Visualization of Crystal Phases in Epitaxial Cathodes via Cepstral Matching of Scanning Nanobeam Electron Diffraction

Kohei Aso[1], Takafumi Kakeya[1], Takumu Tsuchida[1], Hiroki Ito[2], Sho Asano[2], Kenta Watanabe[2], Kazutaka Mitsuishi[3], Koji Kimoto[3], Keisuke Shinoda[3], Takuya Masuda[3*], Masaaki Hirayama[2*], and Yoshifumi Oshima[1*]

1 Japan Advanced Institute of Science and Technology, Ishikawa, 923-1292, Japan,

2 Institute of Science Tokyo, Kanagawa 226-8501, Japan

3 National Institute for Materials Science, Ibaraki, 305-0044, Japan

*Corresponding authors' E-Mail

TM: MASUDA.Takuya@nims.go.jp

MH: hirayama@mct.isct.ac.jp

YO: oshima@jaist.ac.jp

Contents

- Methods, supporting results, and supporting discussions (17 sections)
- Supporting Figures (S1 – S21)

Methods, supporting results, and supporting discussions

Synthesis of epitaxial $LiCoO_2$ cathode

Epitaxial $LiCoO_2$ films were grown on Nb-doped $SrTiO_3$(111) single-crystal substrates (Crystal Base Co., Ltd.). All depositions were conducted using a pulsed-laser-deposition (PLD) system with a KrF excimer laser (wavelength λ = 248 nm, COMPex 201, Lambda Physik) in a vacuum chamber (PLAD-312, AOV Inc.). An electrically conductive $SrRuO_3$ buffer layer was deposited on the substrate from a stoichiometric ceramic target (Toshima Manufacturing Co., Ltd.). $LiCoO_2$ was then deposited from a lithium-rich $Li_{1.3}CoO_2$ target (Toshima Manufacturing Co., Ltd.).

X-ray diffraction (XRD) measurement of the as-grown $LiCoO_2$ film

The as-grown film was measured by XRD (ATX-G, Rigaku). Out-of-plane and in-plane X-ray diffraction (XRD) measurements were conducted to probe lattice planes parallel and perpendicular to the substrate surface, respectively. In both cases, Cu Kα radiation (λ = 1.5406 Å) was monochromated and parallelized to obtain only the Cu Kα_1 line. The out-of-plane scan revealed reflections at approximately 19°, 38°, 59°, and 82°, which were assigned to the 003, 006, 009, and 0012 planes of $LiCoO_2$. In contrast, the in-plane scan exhibited a reflection near 67°, corresponding to the 110 plane of $LiCoO_2$. For both cases, all other observed reflections were attributable to the $SrTiO_3$ substrate and the epitaxially aligned $SrRuO_3$ current collector. Furthermore, the in-plane φ-scan profile revealed equivalent reflections appearing every 60°. This observation suggests that $LiCoO_2$, while intrinsically threefold symmetric around the [001] axis, develops twofold rotational variants with respect to the substrate normal. These results indicate that the $LiCoO_2$ domains grew epitaxially, with the (003) planes oriented parallel to the

$SrTiO_3$(111) planes and with the [100] (or the symmetry-equivalent [$\bar{1}$00]) direction of $LiCoO_2$ aligned parallel to the $SrTiO_3$[$\bar{1}$10] direction.

Scanning electron microscopy (SEM) observation of the as-grown $LiCoO_2$ film

The as-grown film was observed by SEM (Regulus 8230, Hitachi High-Tech) with the acceleration voltage of 10 kV. The SEM image in Figure S1c shows the top view of the pristine sample. The image indicates the dark triangular contrasts and the surrounding bright contrasts. A previous reports suggest the domain morphology was a truncated triangular pyramid with the top $LiCoO_2$(003) and side $LiCoO_2${104} surfaces,[1] which are consistent with the dark and bright contrasts in the SEM image. The triangular features of $LiCoO_2$(003) on the domain surface are aligned at nearly identical angles, suggesting that $LiCoO_2$[100] or $LiCoO_2$[$\bar{1}$00] is aligned with $SrTiO_3$[$\bar{1}$10].

Specimen processing for cross-sectional observations

For scanning transmission electron microscopy (STEM) and scanning nanobeam electron diffraction (SNED) observations, the specimen must be an electron-transparent lamella less than 100 nm thick in the direction of the electron beam. A micrometre-scale cross-section was extracted from the $LiCoO_2$ thin film using a focused Ga-ion beam (FIB; SMI-3050, SII NanoTechnology) operated at 30 kV. Taking the substrate $SrTiO_3$[$\bar{1}$10] orientation and epitaxial relation of $LiCoO_2$ into account, the lift-out was oriented so that the lamella normal (electron beam direction) coincided with the $LiCoO_2$[100] or $LiCoO_2$[$\bar{1}$00] crystallographic direction. Before milling, protective layers were deposited on the film surface to reduce Ga-beam-induced damage, in the order of Ag-doped SiO_2, Ti, and W. Surface polishing was performed with an Ar-ion beam (Gentle Mill, Japan Physitec) at 500 V to remove the Ga-ion-damaged surface layer.

The FIB processing was carried out for the pristine and charge−discharged samples as follows.

STEM observations of as-grown $LiCoO_2$ film

STEM imaging was performed on a JEM-ARM200F (JEOL) operated at 200 kV. Multiple fast frames were positionally aligned and integrated to reduce image distortion and statistical noise.[2–4] Figure S1f and S1g show the atomic-resolution high-angle annular dark-field (HAADF) STEM image of the cross-section sample of the pristine $LiCoO_2$ around the (003) and $(0\bar{1}4)$ surfaces, respectively. Each bright spot in the image corresponds to an atomic column aligned along the electron beam direction or $LiCoO_2$[100]. As HAADF contrast depends on the atomic number, the bright spots represent the atomic columns of Co. The atomic arrangement of Co agrees well with the atomic model of the layered structure shown in Figure S1e. Near the surface, the contrast of Li(003) increases, suggesting the presence of Co. However, the contrast of Li(003) is smaller than that of CoO_2(003), and its thickness is limited to < 1 nm from the outermost surface. Therefore, it is considered that there are Li conduction paths on the surface, and the effect of the Co mixing can be ignored. As described later, the charge-discharge curves were similar to those of layered $LiCoO_2$, supporting our structural characterization.

Battery assembly

2032-type coin cells were assembled in an Ar-filled glovebox using the as-grown $LiCoO_2$ thin film (8 × 8 mm) as the working electrode and lithium-metal foil (Honjo Metal Co., Ltd.) as the counter electrode. A polypropylene separator (Celgard) was thoroughly wetted with an organic electrolyte composed of 1 mol L^{-1} $LiPF_6$ dissolved in a mixed solvent of ethylene carbonate and diethyl carbonate (EC:DEC = 3:7 v/v).

Rate capability measurement

Rate capability measurement was carried out with a potentio-galvanostat (TOSCAT, Toyo System) in the 3.5–4.2 V window (vs Li/Li^+) with different C-rates of 1C, 2C, 5C, 10C, 30C, for 5 cycles each, followed by a C-rate of 1C for 20 cycles. The 1C current was calculated from the theoretical capacity of $LiCoO_2$, together with the film thickness and density determined by X-ray reflectivity and an electrode area of 0.7 cm^2.

The first charge curve displayed a plateau at ~3.9 V, assigned to a two-phase reaction between hexagonal $Li_{0.9}CoO_2$ and $Li_{0.78}CoO_2$, followed by a continuous slope extending to higher voltages (Figure S1a).[5–8] This slope reflects lithium deintercalation through three structural regimes: $Li_{1-x}CoO_2$ with hexagonal ($0.22 \leq x \leq 0.45$), monoclinic ($0.45 \leq x \leq 0.54$), and hexagonal ($0.54 \leq x \leq 0.78$). The small shoulders at 4.1 and 4.2 V arise from the coexistence of those adjacent phase pairs. The discharge capacity was almost maintained even after the rate capability measurement, showing the cycle stability in that voltage range.

High-voltage charge−discharge measurement

Constant-current charge–discharge tests were carried out for the subsequent observations. Except for the voltage window, C-rate, and cycle numbers, the measurement conditions were set similarly to those of the rate capability measurement. The charge−discharge measurement was conducted with the voltage window of 3.5–4.5 V with 1C current for 100 cycles. The first charge−discharge curves show the plateau and small shoulders (Figure S4a), which are similar to the rate capability measurement and previous reports. With cycling, the 4.1 V and 4.2 V shoulders disappeared (Figure S4b), and both discharge capacity and average discharge voltage decreased (Figure S4c−S4d). These features are consistent with previous reports,[5–8] corroborating that the battery in this study worked properly.

SNED acquisition conditions

The SNED observations were performed at an accelerating voltage of 200 kV with a scanning transmission electron microscope (STEM; JEOL JEM-ARM200CF) equipped with a fast pixelated detector (JEOL 4DCanvas). The electron probe was scanned with a dwell time of 500 μsec per probe position. The scan step size was set to ~1.5 nm. The electron dose was calculated from the probe current (measured with the built-in Faraday cup) together with the probe diameter (~0.8 nm, see also main text). Diffraction patterns of 264 × 264 pixels were recorded on a 256 × 256 probe-position grid, generating a four-dimensional data set of ~8GB. The lower half of the scan area, which contains only the $SrTiO_3$ substrate, is omitted from the figures in the main text and Supporting Information.

On the definition of the cepstrum

The amplitude cepstrum $|C(\mathbf{x})|$ of the electron diffraction pattern $I(\mathbf{k})$ can be expressed as:[9,10]

$$|C(\mathbf{x})| = \left|\mathcal{F}\left[\ln\left(I(\mathbf{k})\right)\right]\right| \qquad \text{Eq. S1}$$

where $\mathcal{F}$ denotes the Fourier transform (FT) and $\ln$ represents the logarithmic transform. The variables $\mathbf{x}$ and $\mathbf{k}$ indicate two-dimensional coordinates in real and reciprocal space, respectively. Padgett et al interpreted the electron diffraction pattern $I(\mathbf{k})$ as the squared intensity obtained by physically Fourier transforming the exit wave function $\Phi(\mathbf{x})$ in real space:[9]

$$I(\mathbf{k}) = |\mathcal{F}[\Phi(\mathbf{x})]|^2 \qquad \text{Eq. S2}$$

By substituting Equation S2 into Equation S1, we obtain:

$$|C(\mathbf{x})| = |\mathcal{F}[\ln(|\mathcal{F}[\Phi(\mathbf{x})]|^2)]| \qquad \text{Eq. S3}$$

Equation S3 can be directly compared with the amplitude cepstrum (more commonly referred to as the square root of the power cepstrum) $|C(t)|$ used in the field of audio signal processing:[11]

$$|C(t)| = |\mathcal{F}^{-1}[\ln(|\mathcal{F}[f(t)]|^2)]| \qquad \text{Eq. S4}$$

where $\mathcal{F}^{-1}$ denotes the inverse Fourier transform (IFT) and $f(t)$ is the original time-domain signal.

Although the final FT operation differs between Equation S1 (FT) and Equation S4 (IFT), this discrepancy only results in an intensity scaling factor in the amplitude cepstrum and a sign inversion in the phase cepstrum. In the present method, the amplitude cepstra obtained from both experiments and simulations are normalized during the cross-correlation procedure; therefore, the results remain unaffected by this scaling difference.

Also note that although the cepstrum is sometimes defined through the real part $\mathcal{R}e\,[C(t)]$ in conventional signal processing, we employed the absolute value $|C(\mathbf{x})|$, following prior studies.[9,10] This choice is considered reasonable because (1) the experimental diffraction patterns are often not perfectly even functions due to sample tilt and projection lens misalignment, and (2) the cepstrum is physically associated with interatomic correlations that are expected to be non-negative. Therefore, the use of absolute value provides a robust and physically meaningful representation of the cepstrum in the present context.

Data-processing workflow for generating the cepstrum from the diffraction pattern

The cepstrum-processing procedure is illustrated with an uncalibrated diffraction pattern recorded at a single probe position on $SrTiO_3$ (Figure S3a).[9,10] A small constant intensity (1×10^{-15}) was added to every pixel to avoid singularities when taking the natural logarithm, yielding the log-scaled pattern shown in Figure S3b. To minimize edge-induced artifacts, we introduced

a centered two-dimensional Gaussian window whose peak value is unity and whose 4σ radius matches the image half-width (Figure S3c). The Gaussian-weighted mean intensity was subtracted from the log-pattern, and the result was multiplied element-wise by the window (Figure S3d). This mean-removal step suppresses the window-derived contribution near zero spatial frequency; consequently, the resulting cepstrum has zero intensity at the origin. For finer sampling of the cepstrum, the 264 × 264 windowed array was zero-padded to 512 × 512 by filling the lower-right quadrant with zeros (Figure S3e) and subsequently subjected to a two-dimensional fast Fourier transform. The modulus of the transform constitutes the cepstrum mapped in Figure 1f. Faint vertical and horizontal streaks, attributable to slight dark current or gain mismatch in the pixelated detector, produce spurious peaks along the cepstrum axes. Their influence was mitigated by replacing every pixel below 10 counts with 10 in each pixel in a diffraction pattern (Figure S3g with log-scale intensity), where the threshold is smaller than the maximum signal of ~3000 counts. The corrected Fourier modulus displays reduced spurious spots while preserving the genuine lattice-derived peaks (Figure S3h).

Calibration of diffraction pattern and cepstrum

We calibrated the orientation of each diffraction pattern relative to the probe-scan raster. In the virtual annular dark-field (vADF) image, the $SrTiO_3$(111) plane at the interface runs parallel to the fast-scan (horizontal) direction. The diffraction patterns are taken along the $SrTiO_3[\bar{1}10]$ zone axis and therefore contain the 111 spot. Each diffraction pattern was rotated so that the 111 spot is aligned with the slow-scan (vertical) direction, defining the zero-rotation condition in this study.

The scale of the cepstra was determined from the $SrTiO_3$ substrate. For all probe positions in the lower half of the scan, where only $SrTiO_3$ is present, the cepstra were calculated and averaged

(Figure S4a, left panel). A reference cepstrum was simulated for $SrTiO_3$ with the incident electron beam along $[1\bar{1}0]$ and the [111] direction pointing upward with pixel size 12.2 pm (Figure S4a, center). Experimental and simulated cepstra were converted to log–polar coordinates (Figure S4b), whose vertical and horizontal axes represent to angle and logarithmic radial distance, respectively. The central spot, which includes the experimental influence of thickness and tilt, was masked (Figure S4c). A two-dimensional zero-normalized cross-correlation between the masked log–polar cepstra was then computed. The vertical shift that maximized the correlation gave the residual rotation angle, while the horizontal shift provided the magnification factor. Applying this factor to the simulated cepstrum brought the lattice-derived peaks of both cepstra into register (Figure S4d).

From the measured magnification factor and the known pixel size of the simulation, the pixel size of the experimental cepstrum was estimated to be 15.4 pm. This value indicates a reciprocal-space pixel size of 0.25 nm^{-1} in the original diffraction patterns.

Cepstrum simulations of structural models

Diffraction simulations were carried out for five structural models—layered $LiCoO_2$, quasi-spinel $LiCoO_2$, Co_3O_4 (spinel), CoO (rock salt), and $SrTiO_3$ (cubic).[12] For each model, the resulting nanobeam diffraction patterns were computed using the ReciPro package.[13] Electron scattering was modelled with the Bloch-wave formalism to account for dynamical (multiple) scattering. The convergence semi-angle was fixed at 1.9 mrad, as determined by matching simulated and experimental intensities. The reciprocal-space sampling was set to 0.16 nm^{-1} per pixel. A specimen thickness of 100 nm was assumed in all calculations. To produce model cepstra that could be directly compared with the experimental ones, each simulated pattern was then processed with the same procedure applied to the experimental data.

STEM observations of the high-voltage cycled sample

HAADF STEM imaging was performed for the high-voltage cycled sample. We observed a part of the electrolyte interface areas where phase changes were confirmed by the cepstrum matching analysis (Figure S19). Figure S20 shows the atomic-resolution HAADF images. Note that weak particle-like contrast appears on the $LiCoO_2$; these particles originate from the protective layer for FIB processing, which is sputtered after electrochemical testing. Therefore, they do not cause any structural changes within the LCO cathode. Furthermore, the particles are small (2 nm) and randomly oriented, so their effect on cepstrum matching analysis can be ignored.

In the A1 area of domain A, the atomic arrangement of the domain interior is explained by a layered $LiCoO_2$ arrangement, while the arrangement is different for ~2 nm from the (003) interface (Figure S20a). The Co atoms are arranged more densely, forming an arrangement similar to that of layered $LiCoO_2$ where all Li atoms at (003) have been replaced by Co atoms. This is explained by the rock salt CoO structure (Figure S20b). The cepstrum representing atomic correlations in real space also exhibits a similar pattern (Figure 3c in the main text), demonstrating the validity of the cepstrum transformation.

Domain A's A2 area is near the (012) interface (Figure S20c), and the atomic arrangement also differs by ~2 nm from the interface. At the interface, the bright points indicating Co are divided into bright and dark points. The bright points are represented by rhombuses, indicating the unit cell. Connecting the dark points within forms a bone-like structure, which corresponds to the atomic structure. This pattern corresponds to the spinel Co_3O_4 structure (Figure S20d). At the vertices of the rhombuses in the former, CoO_6 octahedra are densely arranged in the depth direction. On the other hand, at the vertices and nodes of the latter, half of the octahedra are sparsely arranged. Therefore, in the HAADF image, the former appears bright, and the latter appears dark. In the cepstrum, the rhombic unit cell is reflected (Figure 3d in the main text). As

is particularly evident in the A2 area, some of the bright spots are blurred, suggesting a distorted atomic arrangement. This local distortion around the A2 area is considered to be the reason why the correlation coefficient maximum (C_{max}) of spinel is not uniform in the map (Figure 3f in the main text).

Similarly, in the B1 area, both rock salt and spinel types are observed in the area ~2 nm from the interface. These HAADF observation results support the validity of the cepstrum matching analysis.

Supporting discussion on the cepstrum matching analysis results

This section discusses the interpretation of the maps of the correlation coefficient maximum (C_{max}) and the in-plane rotation angle of the cepstrum at which C_{max} occurred (θ_{rot}).

I: $LiCoO_2$ regions

The C_{max} values for the rock salt and spinel phases are lower than those for the layered structure. This may result from several factors, including the small fraction of the rock salt or spinel phases, disorder in the atomic arrangement along the beam direction, and/or cepstral spots coinciding. Single-point cepstra analysis at individual probe positions revealed regions where multiple phases overlap. Atomic-resolution STEM observations of similar regions confirmed the presence of local disorder.

In addition, because several cepstral spots of the layered $LiCoO_2$ structure coincide with those of the rock salt and spinel structures, the C_{max} of the layered phase can appear systematically higher. Furthermore, both the experimental diffraction patterns and the cepstra show that the spinel-related spots are weak, suggesting that the amount of spinel in the specimen is limited.

Within domain A, there is an area where the C_{max} of CoO is slightly higher (Figure 3e in the main text and Figure S15a). Figure S15c shows the average cepstral analysis of this area. Spot arrangement is similar to that of the simulated CoO cepstrum, as marked by R1 and R2. However, the spots are dark and blurred. Therefore, we cannot rule out the possibility of defects other than the presence of the CoO phase.

Inside domain B, there is an area with a slightly higher C_{max} of Co_3O_4. Based on the spot arrangement, it appears to be a layered structure cepstral pattern. Focusing on the intensity ratio, the simulated cepstrum of the layered structure shows that L1 is slightly brighter than L2; however, the experiment shows the opposite. Additionally, the experimental L3 and L4 spots are brighter than the calculated L3 and L4 spots. In the experiment, spots L2, L3, and L4 may have overlapped with spots S1, S2, and S3, respectively, which are observed in the spinel cepstral spectrum. However, we believe that further experiments and simulations are necessary to carefully discuss phase overlap based on cepstral intensity changes.

In the C_{max} map obtained for the simulated spinel cepstrum, there is an area with high values between domains A and B of $LiCoO_2$ (Figure 3f in the main text and Figure S16). The average cepstrum in Figure S16b suggests a high correlation to the spinel cepstrum. However, detailed analysis of the averaged cepstrum reveals that it is generated by the overlap of two layered structures with different in-plane rotation angles.

II: $SrRuO_3$ current collector regions

In Figure 1d (main text), the $SrTiO_3$ and parts of the $SrRuO_3$ display C_{max} values for the simulated cepstrum of the layered $LiCoO_2$. The θ_{rot} map shows almost a uniform angle of ~130º for the corresponding area. These values are attributed to the coincidence of some spots in the experimental and simulated cepstra. The experimental cepstrum of the $SrTiO_3$ (Figure S8i)

shows strong spots with a similar distance from the center to the strong spots in the simulated cepstrum of the layered $LiCoO_2$ (Figure S8j). The spots in the simulated cepstrum of the layered structure match the spots in the experimental spots when the simulated cepstrum is rotated for ~130º counterclockwise. This angle agrees with that at the corresponding area in the θ_{rot} map. The spot coincidence comes from the similar atomic correlation because of the epitaxial relationship.

Some $SrRuO_3$ areas exhibit low C_{max} even for the simulated cepstrum of the cubic $SrTiO_3$ (Figure S7). The averaged diffraction pattern and cepstrum of the corresponding areas show the different patterns from the substrate $SrTiO_3$, respectively. These $SrRuO_3$ areas likely contain defects, different orientations, and/or varying structures. Although spinel contrast appears over the current collector area (Figures 3c and 4 in the main text), its cepstrum also differs from the spinel (Figure S8h). The experimental cepstrum of the $SrRuO_3$ area that has not undergone epitaxial growth has two bright spots (Figure S8h). This partially matches the spinel, resulting in a high C_{max} with the spinel. In addition, the corresponding area shows values of $\theta_{rot} \approx 0º$ or 110º (Figure S14f). When the simulated spinel cepstrum is rotated at this angle, two of the four bright spots in the spinel cepstrum align with the bright spots in the $SrRuO_3$ cepstrum (Figure S16). While other simulation cepstra also share common spots, the spinel has fewer spots, so it is considered that the correlation value becomes particularly high.

III: Vacuum area and protective layers for FIB processing

The vacuum area shows a uniform θ_{rot} of 150º for the layered cepstrum (Figure 1d in the main text). The diffraction pattern of the vacuum area shows a streak (Figure S8a). Considering the diffraction patterns are rotated so that the diffraction patterns and image directions coincide, the streak direction is perpendicular to the detector. Therefore, the streak is attributed to the detector

saturation caused by the strong transmitted electron beam (Figure S5). The streak in the diffraction pattern causes the elongated contrast in the cepstrum. Rotating the layered cepstrum counterclockwise by ~150º matches the elongated contrast. Similarly, the vacuum portion of the θ_{rot} map of cubic $SrTiO_3$ has a uniform value of ~30º, and rotating the calculated cepstrum at this angle matches the elongated contrast. In the rock salt-type θ_{rot} map, the values are roughly 15°, 75°, and 135°, and this can also be explained by the alignment of the spots in the rock salt-type cepstrum. In the case of spinel, the vacuum area has a θ_{rot} of ~150º. The lattice-derived spots in the spinel cepstrum are located at a long distance from the center, rather than the elongated contrast of the vacuum cepstrum. Therefore, it can be considered that the θ_{rot} of ~150º corresponds to the angle at which the weak pattern on the short distance matches the elongated contrast.

The protective layer exhibits a high C_{max} to rock-salt cepstrum locally (Figure 3f in the main text and Figure S15a), likely due to highly crystalline Ti in the protection layer. The high C_{max} value is because ot the nano-sized crystalline grains whose cepstrum correlated with the rock salt-type cepstrum (Figure S15b). There are differences in C_{max} even with similar protection layer areas, probably because the Ti metal is polycrystalline.

As mentioned in the main text, future challenges include the appropriate processing of unknown phases that are not included in candidate cepstra and areas where domains overlap.

Supporting discussion on the dynamical effect on cepstral analysis

The effects of dynamic effects such as thickness and inclination were verified. In the electron diffraction pattern, the intensity in the square area was integrated to obtain the 003 intensity of $LiCoO_2$ in domain A. Figure S shows a map of this integrated intensity for the probe position.

Domains B and C lack contrast, likely due to differences in rotation angle or structure. Domain A shows non-uniform contrast, varying by location. After confirming the position of the transmitted wave from the electron diffraction pattern in the vacuum area, we obtained the average electron diffraction pattern and cepstrum for the dark and bright areas within Domain A in the map. As expected from the map, the 003 diffraction intensity depends on the real-space sample position. Furthermore, each diffraction disk exhibits a distinct pattern, and the patterns of each disk also vary depending on the real-space position. These phenomena are attributed to dynamic effects in electron diffraction.

On the other hand, in the average cepstrum patterns at each real-space position, the lattice-derived spots exhibit similar patterns. As described in the main text, at an acceleration voltage of 200 kV, the radius of the Ewald sphere is large, so the diffraction disk arrangement is determined almost kinematically at the reciprocal lattice points of the crystal lattice. The cepstrum can reduce the effects of dynamics by extracting the periodicity of the disk arrangement.

Implementation of analysis and visualization

Cepstrum matching analysis was performed using proprietary code in the Python programming language with several libraries, such as NumPy[14] for image array operations, OpenCV[15] for cross-correlation calculation, scikit-image[16] for other image processing, and matplotlib[17] for plotting. The VESTA software package was also used to show the crystal models.[18]

Supporting figures

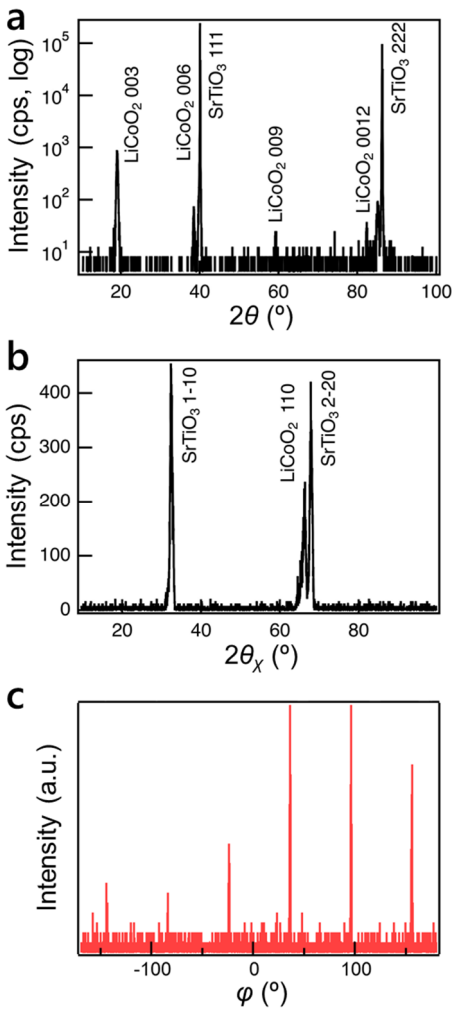


Figure S1. XRD profiles of the as-grown epitaxial $LiCoO_2$ film. **(a)** Out-of-plane, **(b)** in-plane, and **(c)** in-plane φ-scan profiles. The peaks in the out-of-plane and in-plane profiles are refined as $LiCoO_2$ and $SrTiO_3$.

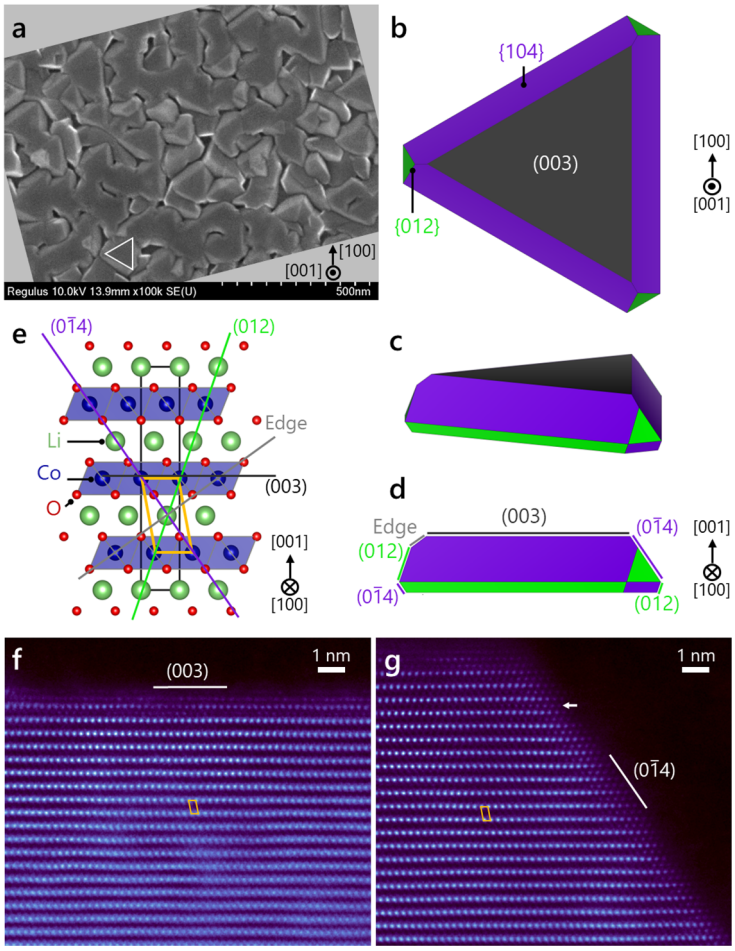


Figure S2. Characterizations of as-grown epitaxial $LiCoO_2$ film synthesized with similar conditions to the film in the main manuscript. **(a)** SEM image of epitaxial $LiCoO_2$ viewed from film normal. The white triangle at the lower left indicates $LiCoO_2$(003). Facet model of the layered $LiCoO_2$ domain of **(b)** top view along [00$\bar{1}$], **(c)** tilt view between e and f, and **(d)** side view along [100]. Black, purple, and green planes indicate (003), (0$\bar{1}$4), and (012) facets, respectively. **(e)** Atomic model of the layered $LiCoO_2$ viewed along [100] to show the relation between the facets and projected atomic arrangement. Green, blue, and red spheres represent Li, Co, and O atoms, respectively. Black, purple, and green lines indicate (003), (0$\bar{1}$4), and (012) facets, respectively, where the facets are viewed in a parallel direction. Orange parallelograms indicate the smallest unit of the projected periodic pattern of layered $LiCoO_2$ viewed along [100]. Atomic-resolution STEM images around **(f)** top (003) and **(g)** side (0$\bar{1}$4) facets. The white leftward arrow indicates the contrast area where a small amount of Co seems mixed into Li(003).

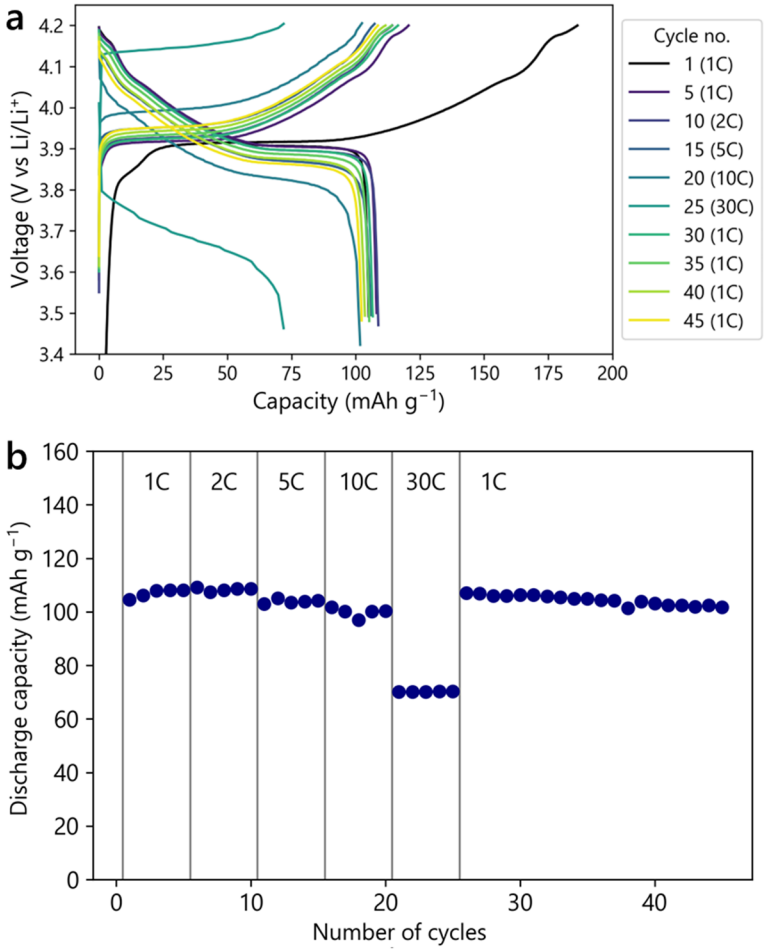


Figure S3. Rate capability measurement of the epitaxial $LiCoO_2$ film that was synthesized at the same time as the film in the main text. **(a)** Charge–discharge curves with C-rate of 1C, 2C, 5C, 10C, and 30C for 5 cycles, followed by 1C for 20 cycles, with the voltage window of 3.5 and 4.2 V (vs Li/Li^+). Small shoulders at 4.1 and 4.2 V are marked by rightward arrows for the charge curve and leftward arrows for the discharged curve. **(b)** Discharge capacity as a function of the number of charge–discharge cycles.

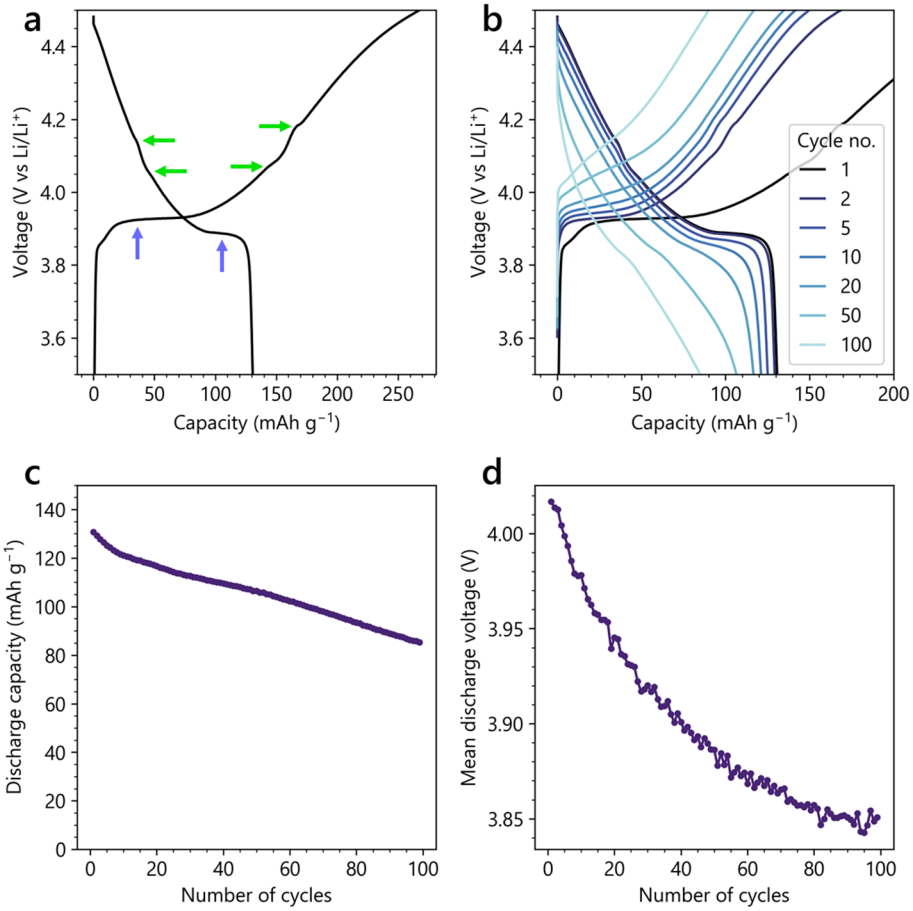


Figure S4. Charge–discharge results of the epitaxial $LiCoO_2$ thin-film that were subsequently analyzed by SNED-cepstral and STEM. **(a)** Charge–discharge curves of the 1st cycle between 3.5 and 4.5 V (vs Li/Li^+) at 1 C. The characteristic 3.9 V plateau is marked by blue upward arrows. Small shoulders at 4.1 and 4.2 V are marked by rightward arrows for the charge curve and leftward arrows for the discharged curve. **(b)** Charge–discharge curves at the 1st, 2nd, 5th, 10th, 20th, 50th, and 100th cycles, respectively. The voltage window was 3.5 to 4.5V, and the C-rate was 1C. **(c)** Discharge capacity and **(d)** mean discharge voltage as a function of the number of charge–discharge cycles.

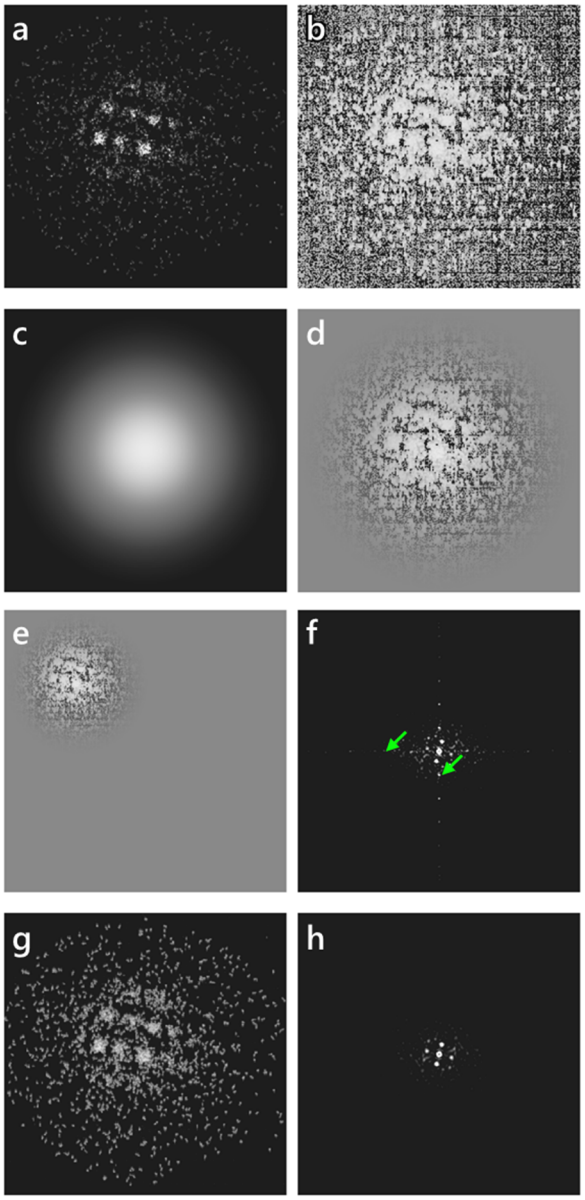


Figure S5. Pre-processing pipeline for cepstrum generation. **(a)** Raw diffraction pattern at a single probe position of the $SrTiO_3$ area. **(b)** Log-intensity diffraction pattern after adding 1×10^{-15} counts to every pixel. **(c)** Centred Gaussian window (peak intensity = 1, background intensity = 0, and 4σ = half-width of the image). **(d)** Log-intensity diffraction pattern with Gaussian-weighted mean removed and window applied. **(e)** Zero-padded pattern to 512×512 pixels^2 for oversampling. **(f)** Cepstrum showing lattice peaks with spurious spots marked by green arrows. **(g)** Log-pattern after replacing all pixels below 10 counts with 10. **(h)** Final cepstrum with spurious spots suppressed.

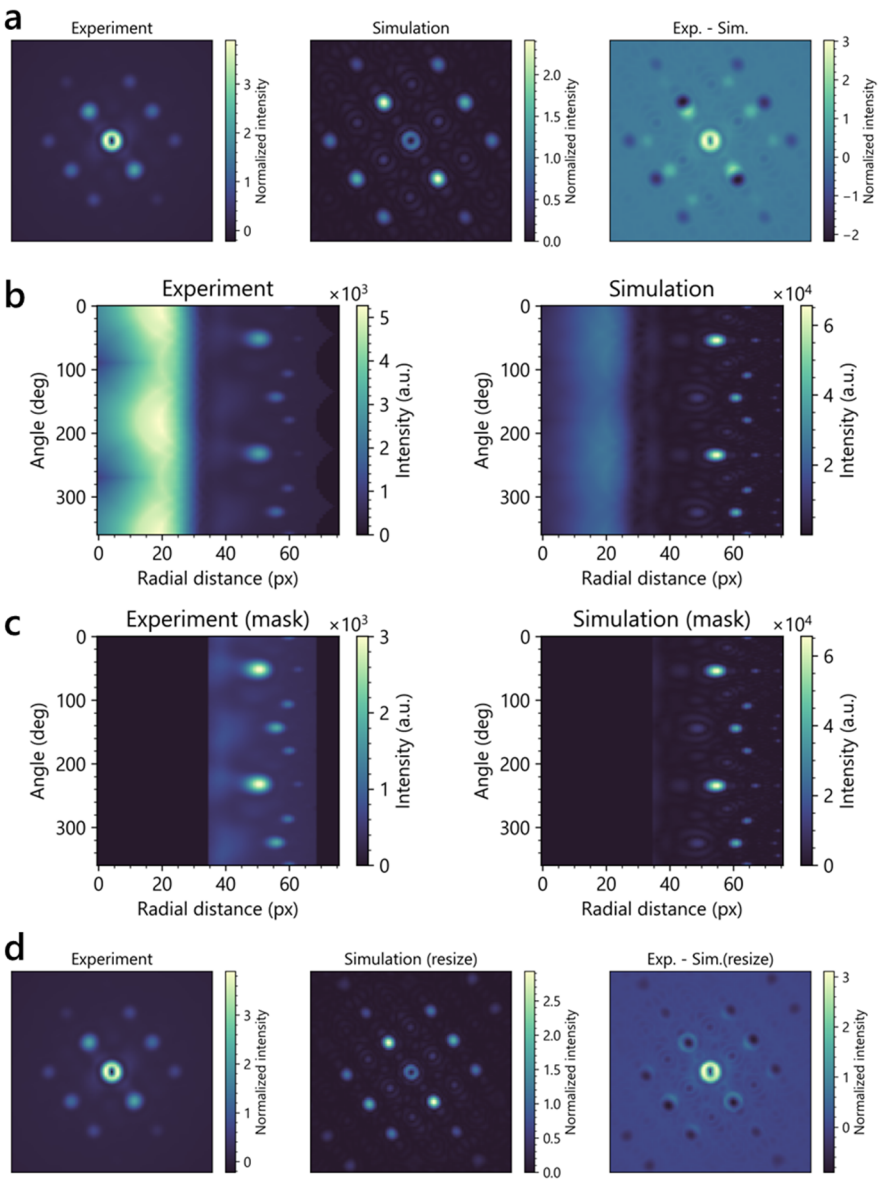


Figure S6. Calibration of pixel size using the $SrTiO_3$ substrate. **(a)** Experimental and simulated $SrTiO_3$ cepstra before calibration. An experimental cepstrum was obtained by averaging the cepstra of the $SrTiO_3$ area. **(b)** Log-polar transformed cepstra. **(c)** Log-polar transformed cepstra, where the short radial distance was masked since it contains the experimental influence. **(d)** Experimental and simulated $SrTiO_3$ cepstra after calibration. The experimental pixel size was obtained from the known pixel size of the simulated cepstrum and magnification ratio.

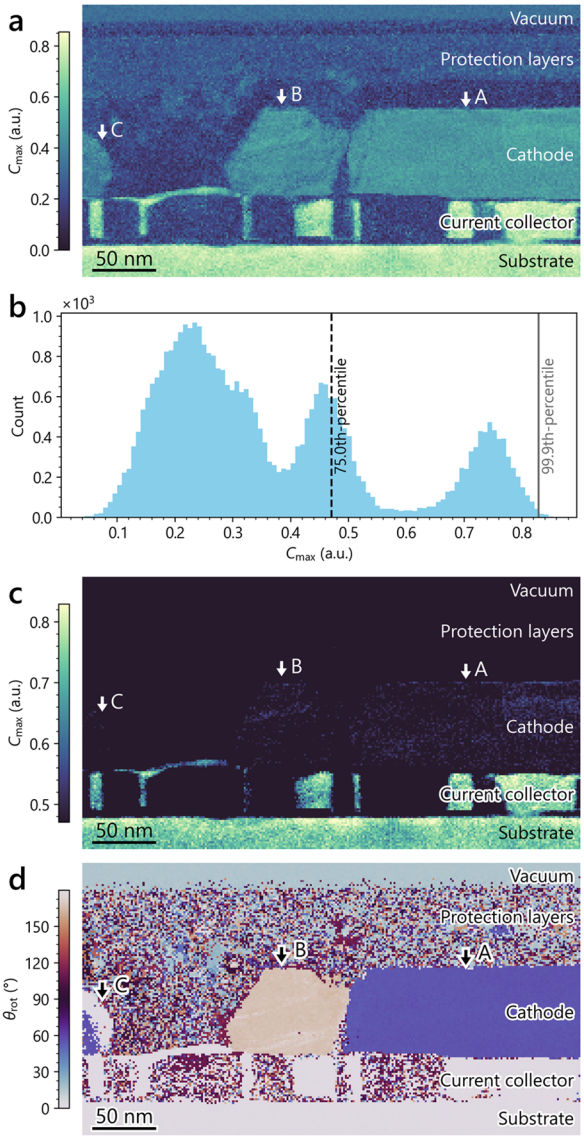
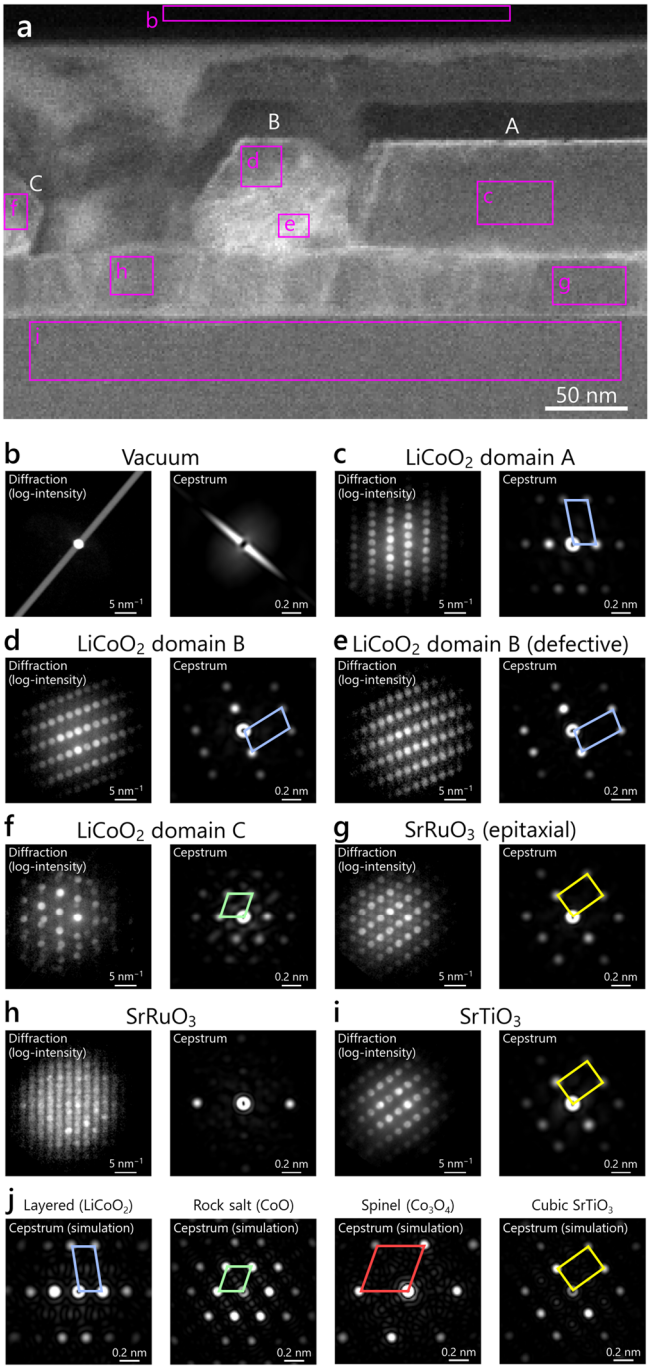


Figure S7. Cepstrum matching analysis relative to the cubic $SrTiO_3$ model. The simulated cepstrum is shown in the right panel in the following Figure S8j. **(a)** Correlation coefficient maximum (C_{max}) map. **(b)** Histogram of C_{max} values. The 75th to 99.9th percentile range was used for the display range. **(c)** Contrast-adjusted C_{max} map. **(d)** Map of the rotation angle θ_{rot} at which C_{max} is attained.



(Caption next page)

Figure S8. The diffraction patterns, cepstrum patterns, and corresponding sample area. The diffraction and cepstrum patterns are averaged for each rectangle area to enhance the signal-to-noise ratio. For each area in **(a)** virtual annular dark field image, averaged diffraction patterns and corresponding cepstra are shown for **(b)** vacuum,**(c)** $LiCoO_2$ domain A, **(d)** $LiCoO_2$ domain B, **(e)** $LiCoO_2$ domain B with line-shaped contrast drop due to the defect, **(f)** $LiCoO_2$ domain C, **(g)** $SrRuO_3$ with cubic structure, **(h)** $SrRuO_3$ with defects, different orientation, and/or different structure, and **(i)** $SrTiO_3$ substrate. **(j)** Simulated cepstra of layered ($LiCoO_2$), rock salt (CoO), spinel (Co_3O_4), and cubic $SrTiO_3$. The blue parallelograms correspond to a projected periodic pattern of layered structure when viewed from the [100] direction. The green and red rhombuses correspond to projected periodic patterns of the rock salt and spinel structure, respectively, when viewed from the $[1\bar{1}0]$ direction. The yellow rectangle corresponds to a projected periodic pattern of the cubic $SrTiO_3$ structure when viewed from the $[\bar{1}10]$ direction.

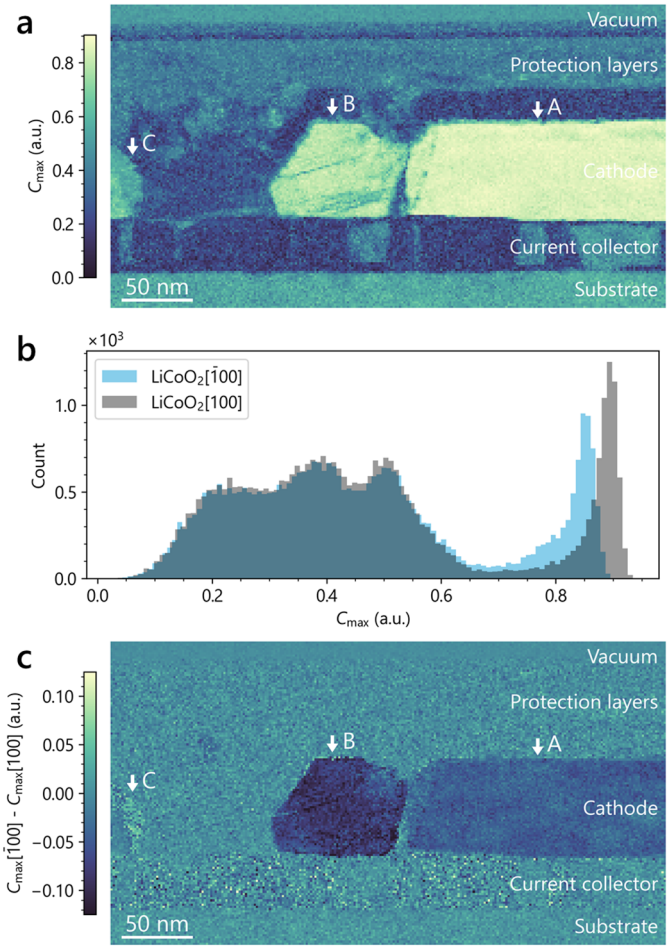


Figure S9. Cepstral matching analysis relative to the simulated cepstrum of $LiCoO_2[\bar{1}00]$, which is the horizontal mirror pattern of the cepstrum of $LiCoO_2[100]$. **(a)** C_{max} map. **(b)** Histogram of C_{max} values. Blue and gray show the C_{max} values of $LiCoO_2[100]$ and $LiCoO_2[\bar{1}00]$, respectively. **(c)** C_{max} difference map, obtained by subtraction of C_{max} of $LiCoO_2[100]$ from C_{max} of $LiCoO_2[\bar{1}00]$, shows negative values in the cathode region, indicating that the C_{max} of $LiCoO_2[100]$ is higher than that of $LiCoO_2[\bar{1}00]$.

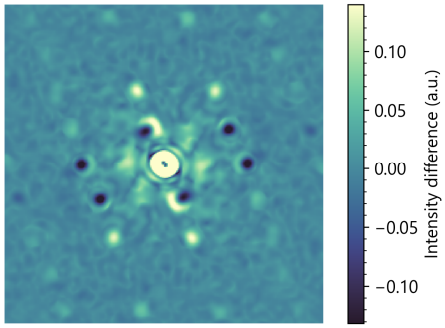


Figure S10. Comparison of cepstra of $LiCoO_2$ domain B between the area of line-shaped contrast drop (Figure S8e) and the other majority part (Figure S8d). The pattern is the cepstrum at the major part subtracted by the contrast drop area; therefore, bright yellow shows the major part, and dark blue shows the contrast drop area. The contrast drop area indicates the layered cepstrum with a shift of ±1/2[120] spots, while the other spots are almost same positions as the major part ones. The major part shows a higher correlation coefficient to the simulation cepstrum. Therefore, the contrast drop area is suggested to include the distorted layered structure, in particular, shear strain.

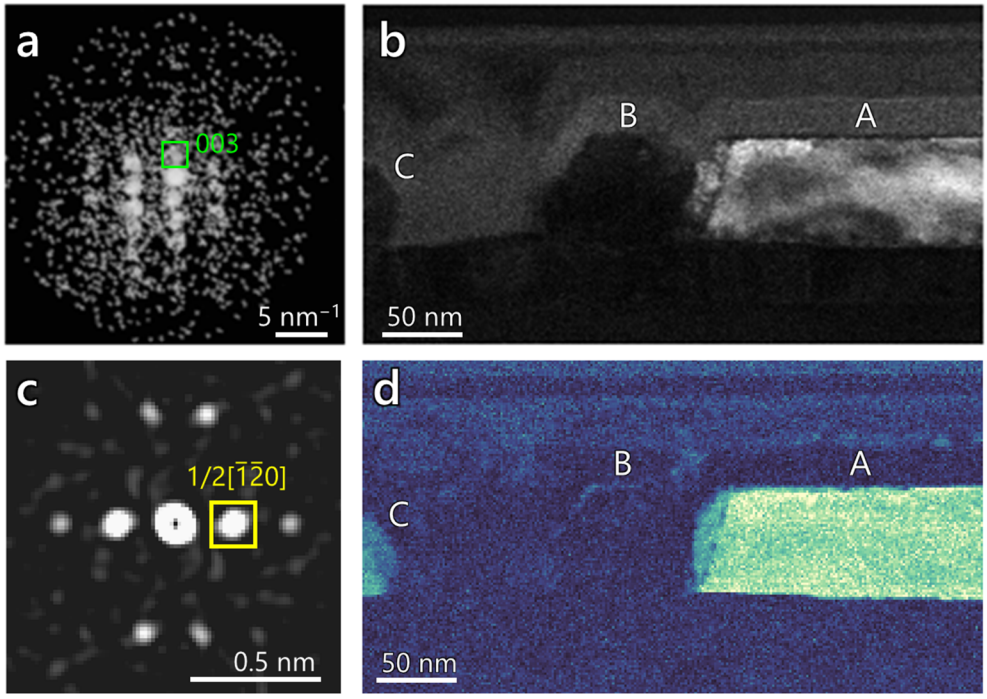


Figure S11. Mapping result of diffraction and cepstrum-spot window. **(a)** Diffraction pattern collected from a single scanning probe position in $LiCoO_2$ domain A. A green rectangle is the intensity integration region around the 003 diffraction disk of layered $LiCoO_2$ of Domain A. **(b)** Map of the 003 intensity at each probe position. Domain A contains intensity variation caused by thickness, tilt, and/or bend. Domain B and C do not show contrast due to the different orientation and structure, as described in detail in the main text. **(c)** Cepstrum collected within $LiCoO_2$ domain A. Yellow rectangle marks the spot corresponding interatomic spacing of layered $LiCoO_2$ along $1/2[\bar{1}\bar{2}0]$. **(d)** Map of the $1/2[\bar{1}\bar{2}0]$ spot intensity at each probe position. In b and d, the depth and upward directions correspond to [100] and [001] of Domain A, respectively. Domain A contains less intensity variation compared to the mapping of diffraction-disk masking. However, domain B does not show contrast due to the different orientation, as described in detail in the main text.

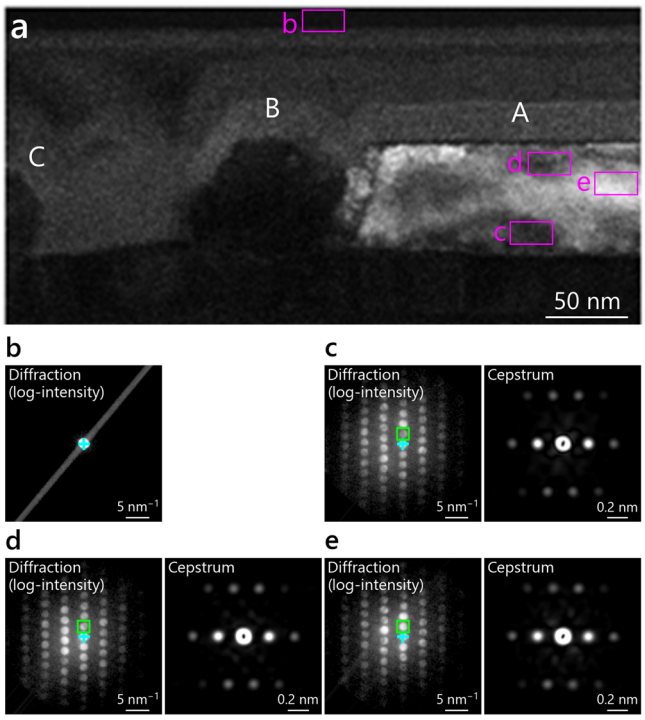


Figure S12. Verification of dynamical diffraction effects. **(a)** Map of the 003 intensity of $LiCoO_2$ of Domain A. **(b)** Diffraction pattern of the vacuum area for confirming the position of the transmitted wave. (**c–d**) Averaged electron diffraction patterns and cepstra for each rectangular area in a.

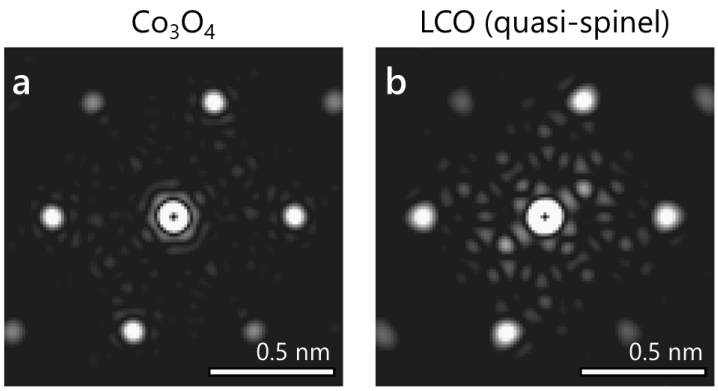


Figure S13. Simulated cepstra of candidate spinel-type phases of **(a)** spinel Co_3O_4 and **(b)** quasi-spinel $LiCoO_2$. The indistinguishable arrangement of spots confirms that these cannot be discriminated by cepstral analysis.

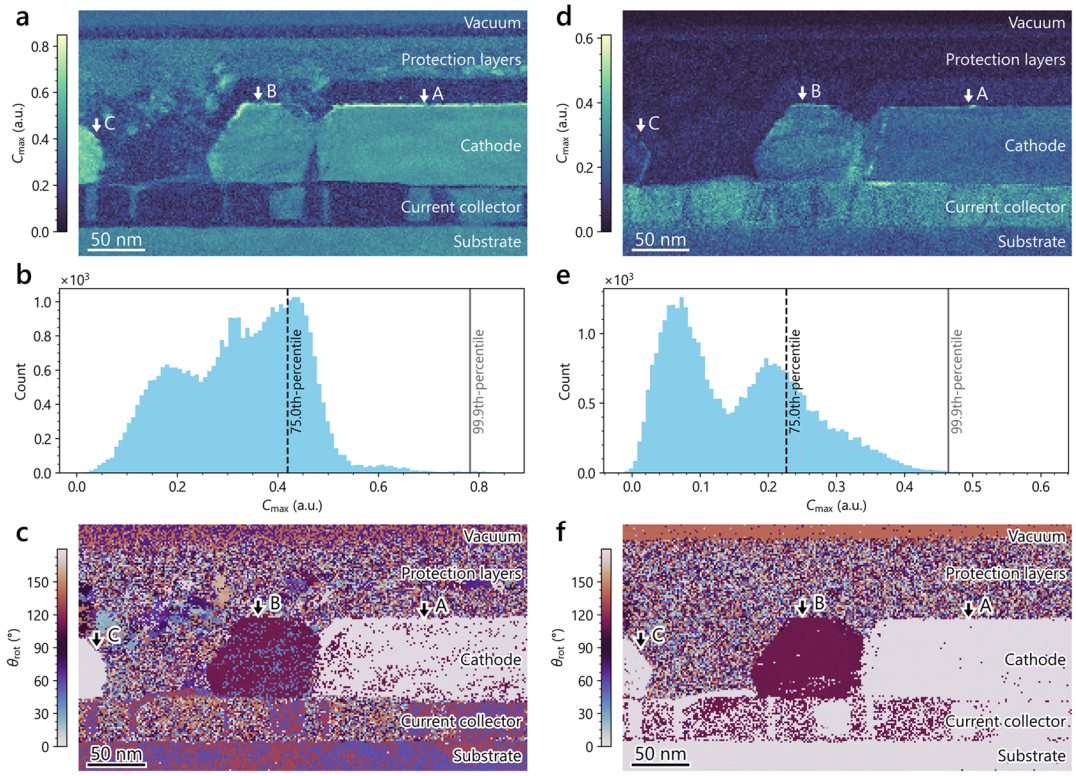


Figure S14. Cepstrum matching analysis relative to the rock salt CoO model and spinel Co_3O_4 model. **(a)** C_{max} map for the simulation cepstrum of the rock salt CoO. **(b)** Histogram of C_{max} values. The 75th to 99.9th percentile range was used for the display range. **(c)** Map of the rotation angle θ_{rot} at which C_{max} is attained. **(d)** C_{max} map for the simulation cepstrum of the spinel Co_3O_4. **(e)** Histogram of C_{max} values. The 75th to 99.9th percentile range was used for the display range. **(f)** Map of the rotation angle θ_{rot} at which C_{max} is attained.

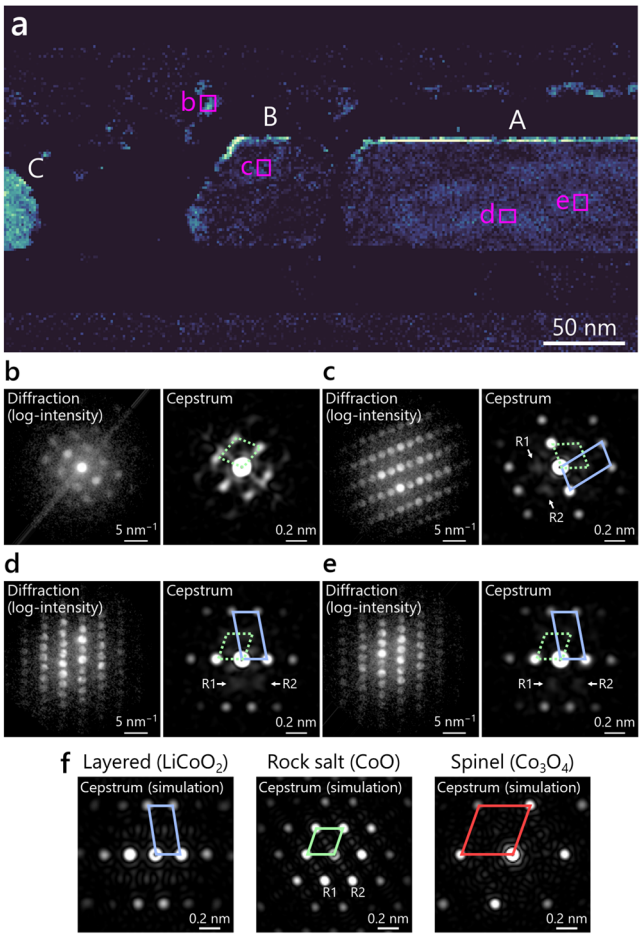


Figure S15. Areas where the C_{max} value is high despite uncertainties regarding the phase of rock salt CoO. **(a)** Threshold-processed C_{max} map for rock salt phase (same as Figure 3e in the main text). **(b–e)** Diffraction patterns and cepstra of the areas surrounded by rectangles in a, where area b may correspond to the Ti metal in the protection layer for FIB, and areas c–d can include defects since the spots at the rock salt positions are weak and blurred. The dotted lines indicate spot patterns that appear similar to those in the rock salt cepstrum, although the phase may not be rock salt. **(f)** Simulated cepstra of layered ($LiCoO_2$), rock salt (CoO), and spinel (Co_3O_4). The blue parallelograms correspond to a projected periodic pattern of layered structure when viewed from the [100] direction. The green and red rhombuses correspond to projected periodic patterns of the rock salt and spinel structure, respectively, when viewed from the $[1\bar{1}0]$ direction. The spots R1 and R2 are labeled for the discussion in the Supporting Information.

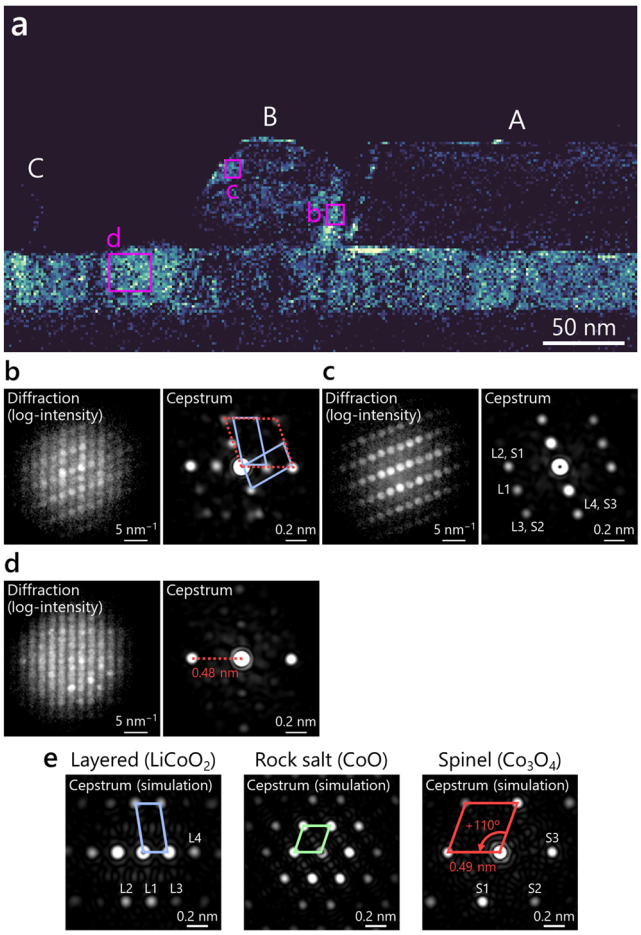


Figure S16. Areas where the C_{max} value is high despite uncertainties regarding the phase of spinel Co_3O_4. **(a)** Threshold-processed C_{max} map for spinel phase (same as Figure 3f in the main text). **(b, c)** Diffraction patterns and cepstra of the areas surrounded by rectangles in a, where area b is the overlapping of layered $LiCoO_2$ peaks with different in-plane rotation angles, and area c is the unidentified area of $SrRuO_3$. The dotted lines indicate spot patterns that appear similar to those in the spinel cepstrum, although the phase may not be rock salt. **(d)** Simulated cepstra of layered ($LiCoO_2$), rock salt (CoO), and spinel (Co_3O_4). The blue parallelograms correspond to a projected periodic pattern of layered structure when viewed from the [100] direction. The green and red rhombuses correspond to projected periodic patterns of the rock salt and spinel structure, respectively, when viewed from the $[1\bar{1}0]$ direction. The spots L1−L4 and S1−S3 are labeled for the discussion in the Supporting Information.

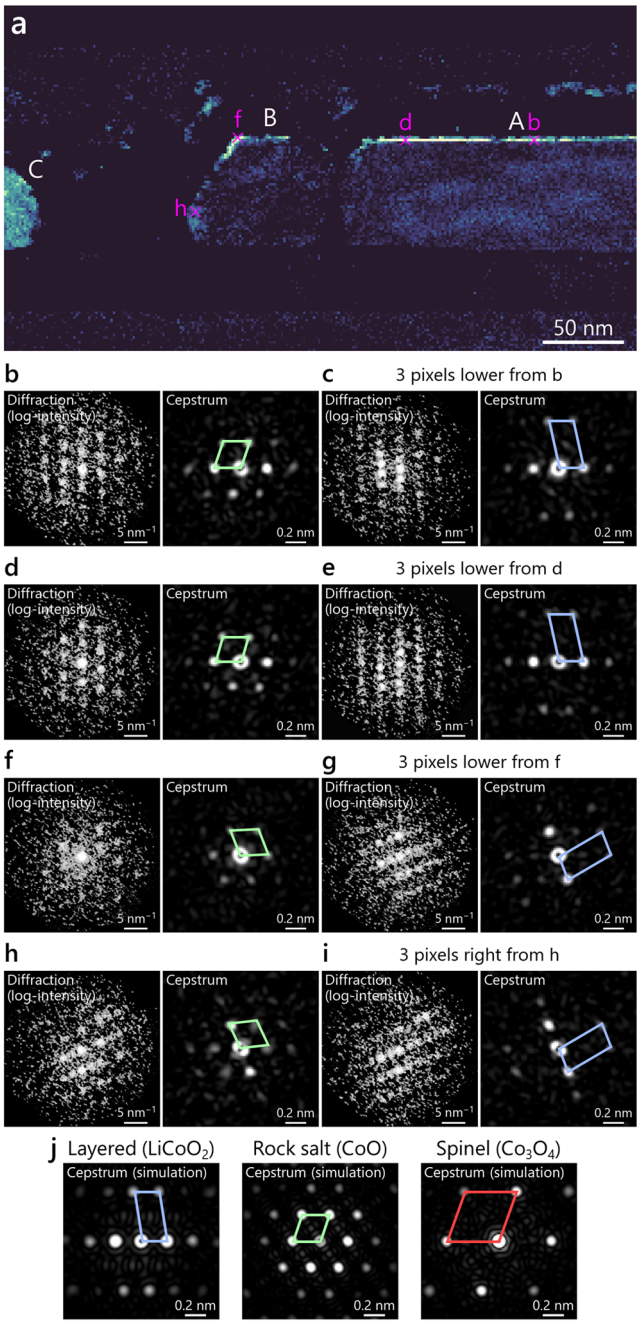


Figure S17. Verification of the C_{max} map for the simulated cepstrum of rock salt phase. **(a)** Threshold-processed C_{max} map for rock salt phase (same as Figure 3e in the main text). **(b, d, f, h)** Diffraction patterns and cepstra of the representative areas showing high C_{max} in the map. **(c, e, g, i)** Diffraction patterns and cepstra 3 pixels lower or right of b, d, f, and h for comparison. **(j)** Simulated cepstra of layered ($LiCoO_2$), rock salt (CoO), and spinel (Co_3O_4). The blue parallelograms correspond to a projected periodic pattern of layered structure when viewed from the [100] direction. The green and red rhombuses correspond to projected periodic patterns of the rock salt and spinel structure, respectively, when viewed from the $[1\bar{1}0]$ direction.

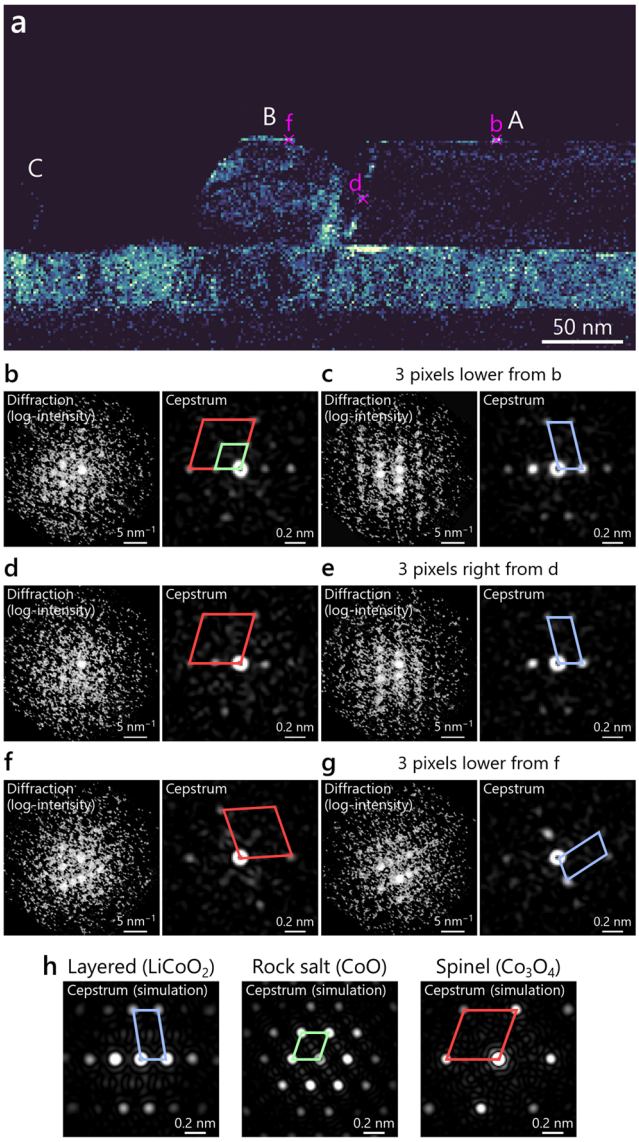


Figure S18. Verification of the C_{max} map for the simulated cepstrum of spinel phase. **(a)** Threshold-processed C_{max} map for spinel phase (same as Figure 3f in the main text). **(b, d, f)** Diffraction patterns and cepstra of the representative areas showing high C_{max} in the map. **(c, e, g)** Diffraction patterns and cepstra 3 pixels lower or right of b, d, f, and h for comparison. **(h)** Simulated cepstra of layered ($LiCoO_2$), rock salt (CoO), and spinel (Co_3O_4). The blue parallelograms correspond to a projected periodic pattern of layered structure when viewed from the [100] direction. The green and red rhombuses correspond to projected periodic patterns of the rock salt and spinel structure, respectively, when viewed from the $[1\bar{1}0]$ direction.

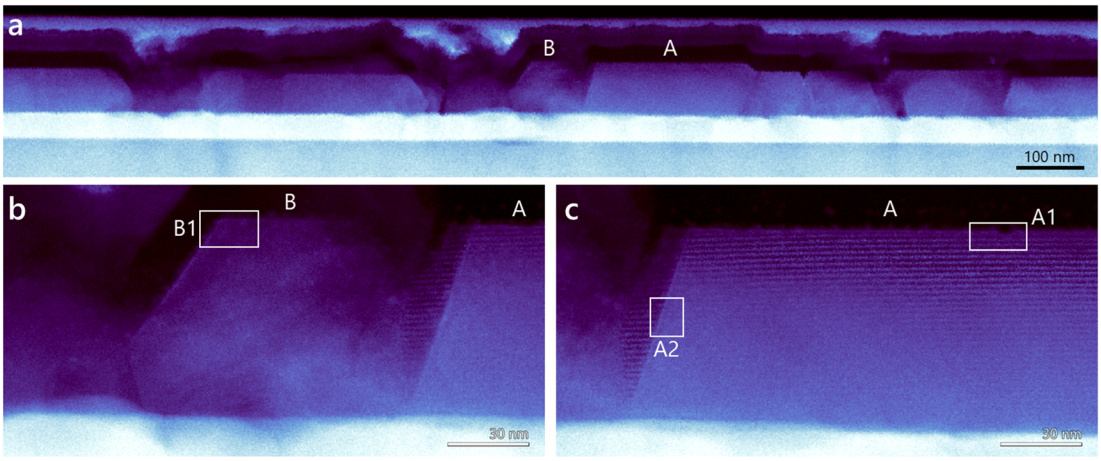


Figure S19. Low-magnification HAADF STEM image around Domains A and B in the high-voltage cycled sample. **(a)** HAADF image of multiple domains, including Domains A and B. Magnified images of Domains **(b)** B and **(c)** A, respectively. The rectangles B1, A1, and A2 show the areas where the following atomic-resolution images were obtained.

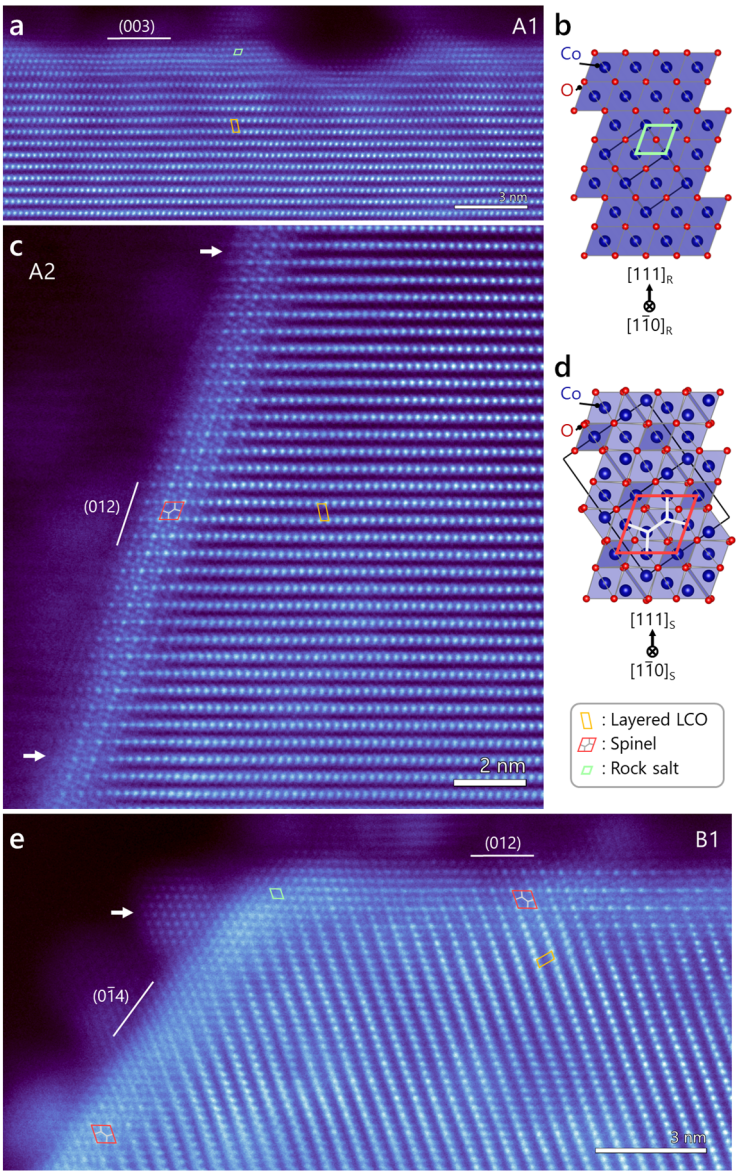


Figure S20. Atomic resolution HAADF image of Domains A and B, where phase transitions were observed by cepstrum matching analysis. (a) (003) interface of Domain A or A1 area in Figure S19c. The outermost interface of ~2 nm shows (b) a CoO-like atomic arrangement. (c) (012) interface of Domain A or A2 area in Figure S19c. Rightward arrows show the blurred spots of Co atomic columns, suggesting the distortion of the atomic arrangement. The outermost interface of ~2 nm shows (d) a Co_3O_4-like atomic arrangement. (e) Edge area including (012) and (0$\bar{1}$4) interfaces of Domain B or B1 area in Figure S19b. The outermost interface of ~2 nm shows a Co_3O_4-like and CoO-like atomic arrangement for (012) and (0$\bar{1}$4) interfaces, respectively. The rightward arrow indicates the nanoparticle in the protection layer for the FIB processing.

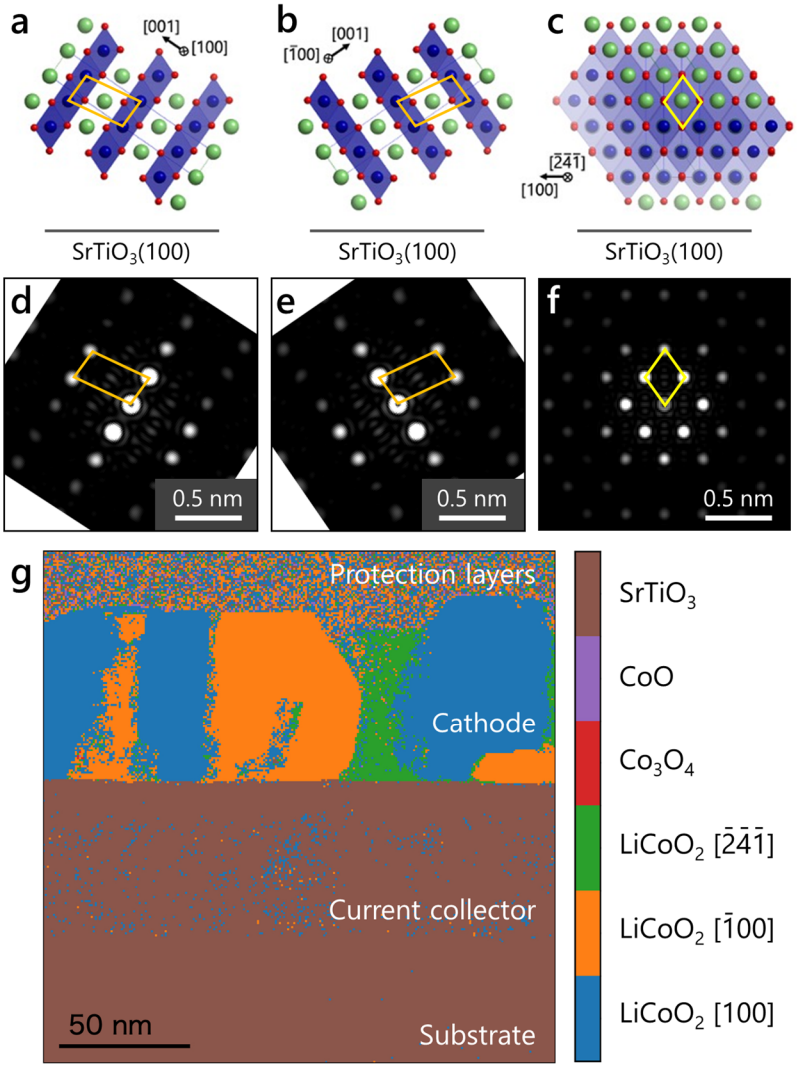


Figure S21. Ongoing cepstrum matching analysis of an as-grown $LiCoO_2${104}/$SrRuO_3$/$SrTiO_3$(100) film. **(a–c)** Atomic models of $LiCoO_2$ considering the three different growth orientations on $SrTiO_3$(100). Note that there is another growth direction of [241] for the depth direction, but it was omitted since its cepstrum cannot be distinguished from that of [$\bar{2}\bar{4}\bar{1}$]. **(d–f)** Simulated cepstra for the three different projection directions of $LiCoO_2$. **(g)** Map resulted from cepstrum matching analysis. C_{max} was compared for six different computational cepstra, and the phase with the highest value was assigned. $LiCoO_2$ domains with three different growth orientations are visualized. Note that although some domains overlap, the overlap cannot be visualized in the map. Also note that the protection layers and a few parts of the current collector show uncertain assignment to $LiCoO_2$. These will be improved in the future.

References

(1) Li, Z.; Yasui, S.; Takeuchi, S.; Creuziger, A.; Maruyama, S.; Herzing, A. A.; Takeuchi, I.; Bendersky, L. A. Structural Study of Epitaxial $LiCoO_2$ Films Grown by Pulsed Laser Deposition on Single Crystal $SrTiO_3$ Substrates. *Thin Solid Films* **2016**, *612*, 472–482. https://doi.org/10.1016/j.tsf.2016.05.017.

(2) Aso, K.; Higashimine, K.; Miyata, M.; Kamio, H.; Oshima, Y. Three-Dimensional Atomic-Scale Characterization of Titanium Oxyhydroxide Nanoparticles by Data-Driven Lattice Correlation Analysis. *Commun Chem* **2025**, *8* (1), 122. https://doi.org/10.1038/s42004-025-01513-2.

(3) Aso, K.; Oshima, Y. Precise Positional Alignment of Atom-Resolved HAADF Images of Heteroepitaxial Interface with Low Signal-to-Noise Ratio. *Microscopy* **2025**, *74* (1), 57–62. https://doi.org/10.1093/jmicro/dfae038.

(4) Aso, K.; Maebe, J.; Tran, X. Q.; Yamamoto, T.; Oshima, Y.; Matsumura, S. Subpercent Local Strains Due to the Shapes of Gold Nanorods Revealed by Data-Driven Analysis. *ACS Nano* **2021**, *15* (7), 12077–12085. https://doi.org/10.1021/acsnano.1c03413.

(5) Hata, J.; Hirayama, M.; Suzuki, K.; Dupré, N.; Guyomard, D.; Kanno, R. Effect of Surface Chemical Bonding States on Lithium Intercalation Properties of Surface-Modified Lithium Cobalt Oxide. *Batteries & Supercaps* **2019**, *2* (5), 454–463. https://doi.org/10.1002/batt.201800122.

(6) Amatucci, G. G. CoO_2, The End Member of the Li_xCoO_2 Solid Solution. *J. Electrochem. Soc.* **1996**, *143*.

(7) Ohzuku, T.; Ueda, A. Solid-State Redox Reactions of $LiCoO_2$ (R-3m) for 4 Volt Secondary Lithium Cells. *J. Electrochem. Soc.* **1994**, *141* (11), 2972–2977. https://doi.org/10.1149/1.2059267.

(8) Reimers, J.; Dahn, J. Electrochemical and In Situ X-Ray Diffraction Studies of Lithium Intercalation in Li_xCoO_2. *Journal of The Electrochemical Society* **1992**, *139*, 2091–2097.

(9) Padgett, E.; Holtz, M. E.; Cueva, P.; Shao, Y.-T.; Langenberg, E.; Schlom, D. G.; Muller, D. A. The Exit-Wave Power-Cepstrum Transform for Scanning Nanobeam Electron Diffraction: Robust Strain Mapping at Subnanometer Resolution and Subpicometer Precision. *Ultramicroscopy* **2020**, *214*, 112994. https://doi.org/10.1016/j.ultramic.2020.112994.

(10) Holtz, M. E.; Padgett, E.; Johnston-Peck, A. C.; Levin, I.; Muller, D. A.; Herzing, A. A. Mapping

Polar Distortions Using Nanobeam Electron Diffraction and a Cepstral Approach. *Microscopy and Microanalysis* **2023**, *29* (4), 1422–1435. https://doi.org/10.1093/micmic/ozad070.

(11) Oppenheim, A. V.; Schafer, R. W. From Frequency to Quefrency: A History of the Cepstrum. *IEEE Signal Processing Magazine* **2004**, *21* (5), 95–106. https://doi.org/10.1109/MSP.2004.1328092.

(12) Jain, A.; Ong, S. P.; Hautier, G.; Chen, W.; Richards, W. D.; Dacek, S.; Cholia, S.; Gunter, D.; Skinner, D.; Ceder, G.; Persson, K. A. Commentary: The Materials Project: A Materials Genome Approach to Accelerating Materials Innovation. *APL Materials* **2013**, *1* (1), 011002. https://doi.org/10.1063/1.4812323.

(13) Seto, Y.; Ohtsuka, M. *ReciPro* : Free and Open-Source Multipurpose Crystallographic Software Integrating a Crystal Model Database and Viewer, Diffraction and Microscopy Simulators, and Diffraction Data Analysis Tools. *J Appl Crystallogr* **2022**, *55* (2), 397–410. https://doi.org/10.1107/S1600576722000139.

(14) Harris, C. R.; Millman, K. J.; van der Walt, S. J.; Gommers, R.; Virtanen, P.; Cournapeau, D.; Wieser, E.; Taylor, J.; Berg, S.; Smith, N. J.; Kern, R.; Picus, M.; Hoyer, S.; van Kerkwijk, M. H.; Brett, M.; Haldane, A.; del Río, J. F.; Wiebe, M.; Peterson, P.; Gérard-Marchant, P.; Sheppard, K.; Reddy, T.; Weckesser, W.; Abbasi, H.; Gohlke, C.; Oliphant, T. E. Array Programming with NumPy. *Nature* **2020**, *585* (7825), 357–362. https://doi.org/10.1038/s41586-020-2649-2.

(15) Bradski, G. The OpenCV Library. *Dr. Dobb's Journal of Software Tools* **2000**.

(16) Van Der Walt, S.; Schönberger, J. L.; Nunez-Iglesias, J.; Boulogne, F.; Warner, J. D.; Yager, N.; Gouillart, E.; Yu, T. Scikit-Image: Image Processing in Python. *PeerJ* **2014**, *2014* (1), 1–18. https://doi.org/10.7717/peerj.453.

(17) Hunter, J. D. Matplotlib: A 2D Graphics Environment. *Computing in Science & Engineering* **2007**, *9* (3), 90–95. https://doi.org/10.1109/MCSE.2007.55.

(18) Momma, K.; Izumi, F. *VESTA 3* for Three-Dimensional Visualization of Crystal, Volumetric and Morphology Data. *Journal of Applied Crystallography* **2011**, *44* (6), 1272–1276. https://doi.org/10.1107/S0021889811038970.